

Electrically Tunable Conductance and Edge Modes in Topological Crystalline Insulator Thin Films: Tight-Binding Model Analysis

Motohiko Ezawa

Department of Applied Physics, University of Tokyo, Hongo 7-3-1, 113-8656, Japan

We propose a minimal tight-binding model for thin films made of topological crystalline insulator (TCI) on the basis of the mirror and discrete rotational symmetries. The basic term consists of the spin-orbit interaction describing a Weyl semimetal, where gapless Dirac cones emerge at all the high symmetry points in the momentum space. We then introduce the mass term providing gaps to Dirac cones at our disposal. They simulate the thin films made of the [001], [111] and [110] TCI surfaces. TCI thin films are topological insulators protected by the mirror symmetry. We analyze the mirror-Chern number, the edge modes and the conductance by breaking the mirror symmetry with the use of electric field. We propose a multi-digit topological field-effect transistor by applying electric field independently to the right and left edges of a nanoribbon. Our results will open a new way to topological electronics.

Topological insulator is one of the most fascinating concept found in this decade^{1,2}. Recent flourish of the study of topological insulator is based on the finding of the time-reversal invariant topological insulator³⁻⁵. Very recently, a new class of topological insulator, topological crystalline insulator (TCI), attracts much attention⁶⁻²⁰. The best example is given by $\text{Pb}_x\text{Sn}_{1-x}\text{Te}$, which has been found to be a TCI experimentally⁸⁻¹⁰. There are three types of the surface states, the [001], [111] and [110] surfaces, which have discrete rotation symmetries C_N with $N = 4, 6$ and 2 , respectively. Gapless Dirac cones emerge inevitably on the surface of a topological insulator. Indeed, it has been experimentally observed that there are gapless Dirac cones at the X and Y points in the [001] surface⁸⁻¹⁰, and at the Γ and three M points in the [111] surface^{11,12}. Theoretical studies have been performed with the use of first-principle calculation and low-energy effective Dirac theory.

Although there are yet no experimental measurements, theoretical studies^{13,14} have been presented also on the thin film made of a TCI. It is characterized by the same discrete rotation symmetry C_N , and additionally by the mirror symmetry about the 2D plane. When the film is thin enough, a gap opening occurs due to hybridization between the front and back surfaces, and it turns the system into a topological insulator. Now, electronics is based on circuits in two dimensions. It is important and urgent to make a further investigation of a TCI thin film, since it may well be a good candidate for designing nanodevices in topological electronics.

The TCI thin film is a topological insulator protected by the mirror-symmetry. Accordingly the topological number is the mirror-Chern number^{21,22}. A prominent feature is that we can break the mirror symmetry simply by applying external electric field. This is highly contrasted to the case of the time-reversal invariant topological insulator, where the time-reversal breaking should be caused by magnetic field or exchange field induced by ferromagnet. Magnetic field and exchange field are hard to control precisely. On the other hand, a precise control of the electric field is possible within current technique.

The aim of this work is to explore the physics of the TCI thin film by constructing a minimal tight-binding model based

on the discrete rotation symmetry C_N and the mirror symmetry about the 2D plane. The tight-binding model is essential to make a deeper understanding of the system, which is not attained by first-principle calculation and low-energy effective Dirac theory. For instance, according to the low-energy theory¹³, the [001] thin film made of $\text{Pb}_x\text{Sn}_{1-x}\text{Te}$ has two Dirac cones at the X and Y points, where the chirality is identical. However, the Nielsen-Ninomiya theorem²³ dictates that the total chirality is zero. Consequently, there must be two additional Dirac cones with the chirality opposite to that of the X and Y points. In our tight-binding model these two Dirac cones emerge at the Γ and M points, though they are removed from the low-energy spectrum. The tight-binding model is also useful to analyze the edge states, which transport the ordinary electric current reflecting the topological properties of the thin film.

We start with a system where the spin-orbit interaction (SOI) dominates the transfer term. We demonstrate that such a system is a Weyl semimetal consisting of multiple Dirac cones at all the high symmetric points. We next introduce mass terms to give gaps to Dirac cones at our disposal. The system may well describe the TCI thin film made of $\text{Pb}_x\text{Sn}_{1-x}\text{Te}$ with an appropriate choice of phenomenological mass parameters. Then we break the mirror symmetry by introducing a perpendicular electric field E_z . The conductance is calculated in the presence of E_z . The conductance is switched off by the electric field. Namely, it acts as a topological field-effect transistor²⁴. By attaching two independent gates to the sample, we can separately control the right and left edge states. The conductance can be 0, 1 and 2, which forms a multi-digit topological field-effect transistor, where the conductance is quantized and topologically protected. Our results open a new way to electric-field controllable topological electronics.

Main Results

Our main results consist of a phenomenological construction of minimal tight-binding Hamiltonians for the TCI thin film, and the analysis of electrically controllable conductance and edge modes of a nanoribbon in view of the bulk-edge correspondence.

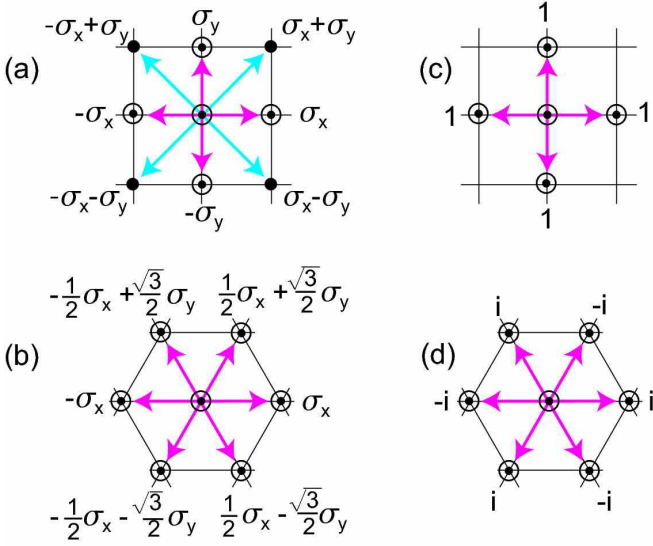


FIG. 1: **Nearest and next-nearest neighbor sites in real space.** We give the value of $\sigma \cdot \mathbf{d}_{ij}^\ell$ for the nearest ($\ell = 1$, magenta) and next-nearest ($\ell = 2$, cyan) neighbor sites for the square lattice (a) and the triangular lattice (b) in the Hamiltonian (2). We also give the value of ν_{ij} for the nearest neighbor site ($\ell = 1$, magenta) for the square lattice (c) and the triangular lattice (d) in the Hamiltonian (7).

Tight-binding Hamiltonians. The SOI plays a key role in the physics of topological insulators. We consider a model where the SOI dominates the system. A simplest example would be the Rashba SOI,

$$H_{\text{SO}} = i \sum_{\ell=1} \lambda_\ell \sum_{\langle i,j \rangle} c_i^\dagger [\sigma \times \mathbf{d}_{ij}^\ell] c_j. \quad (1)$$

Alternatively we may think of

$$H_{\text{SO}} = i \sum_{\ell=1} \lambda_\ell \sum_{\langle i,j \rangle} c_i^\dagger [\sigma \cdot \mathbf{d}_{ij}^\ell] c_j, \quad (2)$$

or even take a sum of them. Here, $\sigma = (\sigma_x, \sigma_y, \sigma_z)$ represents the Pauli matrix for the spin, and $\mathbf{d}_{ij}^\ell = \mathbf{r}_i - \mathbf{r}_j$ connects a pair of the ℓ -th nearest neighbor sites i and j in the lattice with λ_ℓ the coupling strength. As is easily shown, the results based on the Hamiltonian (1) are obtained from those on the Hamiltonian (2) simply with the replacement of a set of momenta (k_x, k_y) by $(k_y, -k_x)$. Furthermore, the low-energy theory derived from a first-principle calculation¹³ supports the choice of (2). Hence we concentrate on (2) hereafter.

Let N_ℓ be the number of the ℓ -th neighbor sites. In the momentum representation the Hamiltonian is rewritten as

$$H_{\text{SO}} = \sum_{\mathbf{k}} c^\dagger(\mathbf{k}) \hat{H}_{\text{SO}}(\mathbf{k}) c(\mathbf{k}), \quad (3)$$

with

$$\hat{H}_{\text{SO}}(\mathbf{k}) = \sum_{\ell=1} \lambda_\ell \sum_{n=1}^{N_\ell} \sigma \cdot \mathbf{d}_n^\ell e^{i\mathbf{d}_n^\ell \cdot \mathbf{k}}, \quad (4)$$

where \mathbf{d}_{ij}^ℓ is determined by requiring the invariance under the discrete rotational symmetry C_N . (See the Methods with respect to C_N .) For instance, \mathbf{d}_n^ℓ for the nearest neighbor sites ($\ell = 1$) is expressed as

$$\mathbf{d}_n^1 = |\mathbf{d}_n^1| (\cos \theta_n, \sin \theta_n), \quad \theta_n = \frac{2\pi n}{N} \quad (5)$$

for the triangular ($N = 3$) and square ($N = 4$) lattices: See Fig.1(a) and (c). We shall soon see that this model has multiple Dirac cones at the high symmetry points known such as the X , Y , Γ and M points in the square lattice and the Γ , K , K' , M_1 , M_2 , M_3 points in the triangular lattice. Thus the Hamiltonian (1) describes a Weyl semimetal.

The minimal tight-binding Hamiltonian of a TCI thin film would be a four-band model due to the spin and pseudospin (surface) degrees of freedom. Let $\tau = (\tau_x, \tau_y, \tau_z)$ be the Pauli matrix to describe the pseudospin representing the front ($\tau_z = 1$) and back ($\tau_z = -1$) surfaces. When the film is thin enough, the symmetric state becomes the ground state, opening a gap to all Dirac cones due to hybridization. We employ the Hamiltonian (1) to describe the symmetric state. Furthermore we apply the electric field E_z between the two surfaces.

These effects are realized by considering the four-band effective tight-binding Hamiltonian,

$$\hat{H} = \hat{H}_{\text{SO}} \tau_y + \hat{H}_m \tau_x + E_z \tau_z, \quad (6)$$

together with \hat{H}_{SO} given by (4) and \hat{H}_m obtained from

$$H_m = \sum_{\ell=0} m_\ell \sum_{\langle i,j \rangle} \nu_{ij}^\ell c_i^\dagger c_j, \quad (7)$$

where ν_{ij}^ℓ is a number characteristic to the lattice structure and determined by the vector \mathbf{d}_{ij}^ℓ so as to preserve the crystalline symmetry, and i, j runs over the ℓ -th nearest neighbor sites. We take $\nu_{ij}^0 = \delta_{ij}$ and show ν_{ij}^1 in Fig.1(c) and (d) for the square and triangular lattices. As we shall soon see, the gap at each Dirac point is adjusted by choosing the mass parameters m_ℓ appropriately.

In the absence of the external electric field ($E_z = 0$), the Hamiltonian (6) is invariant under the mirror symmetry about the 2D plane,

$$M H(\mathbf{k}) M^{-1} = H(\mathbf{k}), \quad (8)$$

where the mirror operator is given by

$$M = -i\sigma_z \tau_x. \quad (9)$$

The mirror symmetry is broken by the external electric field ($E_z \neq 0$) as

$$M(E_z \tau_z) M^{-1} = -E_z \tau_z. \quad (10)$$

When the system is an insulator, the mirror-Chern charge is defined and calculable even for $E_z \neq 0$ according to a general scheme²⁵.

Square lattice with C_4 symmetry. We first consider the square lattice with the C_4 symmetry. Let us set $E_z = 0$. First,

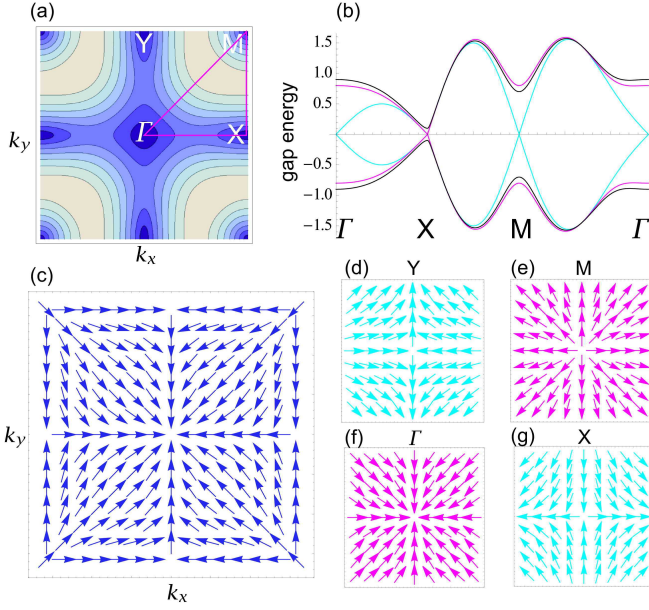


FIG. 2: **Band structure and spin direction on square lattice.** (a) We present a contour plot of the band structure of the Hamiltonian (6) on the square lattice. We have set $\lambda_1 = \lambda_2 = 0$, $m_1 = m_2 = 0$. The energy is lower in darker region. (b) We give the band structure along the lines shown in magenta in (a). We have set $\lambda_1 = \lambda_2 = 0$ in all three curves. Cyan curves are with $m_1 = m_2 = 0$. Magenta curves are with $m_1 = m_2 = 0.4$, $m_0 = 0$. Black curves are with $m_1 = m_2 = 0.4$, $m_0 = 0.1$. (c) We show the spin direction in the thin film with the C_4 symmetry for the whole Brillouin zone, around (d) the Y point, (e) the M point, (f) the Γ point and (g) the X point. The spin structure is hedgehog-like around the Γ and M points with the opposite directions, both yielding the positive chirality (magenta), while it is anti-hedgehog-like around the X and Y points with the opposite directions, both yielding the negative chirality (cyan). They contribute to the mirror-Chern number.

taking the contributions from the nearest neighbor sites ($\ell = 1$) and the next-nearest neighbor sites ($\ell = 2$), we obtain from the Hamiltonian (2) as

$$\hat{H}_{\text{SO}} = A_x \sigma_x + A_y \sigma_y \quad (11)$$

with

$$A_x = \lambda_1 \sin k_x + \lambda_2 \sin k_x \cos k_y, \quad (12a)$$

$$A_y = \lambda_1 \sin k_y + \lambda_2 \sin k_y \cos k_x. \quad (12b)$$

See the illustration in Fig.1(a) and (b). The energy spectrum is given by

$$E = \pm \sqrt{A_x^2 + A_y^2}. \quad (13)$$

There are gapless Dirac cones at the X, Y, Γ and M points, as illustrated in Fig.2, where the band structure is shown. The Hamiltonian describes a Weyl semimetal.

The effective low-energy Hamiltonian is given by (11) near each Dirac point with

$$A_x = v_x \tilde{k}_x, \quad A_y = v_y \tilde{k}_y, \quad (14)$$

where v_x and v_y are the velocities

$$v_x = n_x(\lambda_1 + n_y \lambda_2), \quad v_y = n_y(\lambda_1 + n_x \lambda_2), \quad (15)$$

and \tilde{k}_x and \tilde{k}_y are the renormalized momenta

$$\tilde{k}_x = k_x + \frac{n_x - 1}{2} \pi, \quad \tilde{k}_y = k_y + \frac{n_y - 1}{2} \pi, \quad (16)$$

as follows from (12). A set of numbers (n_x, n_y) is $(-1, 1)$ for X, $(1, -1)$ for Y, $(1, 1)$ for Γ , $(-1, -1)$ for M. The chirality of the Dirac cone is given by $n_x n_y$ at each point. An anisotropy ($v_x \neq v_y$) has been introduced into the system by introducing the nearest and next-nearest neighbor contributions ($\lambda_1 \neq 0, \lambda_2 \neq 0$).

We illustrate the spin direction around each Dirac point in Fig.2. The spin direction yields one negative chirality at the X and Y points apiece, while it yields one positive chirality to the Γ and M points apiece. The total chirality is zero over the Brillouin zone, as required by the Nielsen-Ninomiya theorem²³.

We proceed to consider the total Hamiltonian (6) with $E_z = 0$, which reads

$$\hat{H} = [A_x \sigma_x + A_y \sigma_y] \tau_y + m \tau_x, \quad (17)$$

with (12) and

$$m = m_0 + m_1(\cos k_x + \cos k_y). \quad (18)$$

The energy spectrum is now given by

$$E = \pm \sqrt{A_x^2 + A_y^2 + m^2}. \quad (19)$$

We see that m_1 opens a gap at the Γ and M points, while m_0 opens a gap at all Dirac points, as illustrated in Fig.2(b). Note that, if we set $m_0 = 0$, massless Dirac cones appear at the X and Y points [Fig.2(b)]. The term $m_0 \tau_x$ is understood to simulate the effect of a gap opening due to hybridization between the front and back surfaces in a thin film. The Dirac cones at the Γ and M points are removed from the low-energy theory when we take a large value of m_1 .

The low-energy Dirac theory is extracted from (17) around the X and Y points as

$$H_X = (v_1 k_x \sigma_x - v_2 k_y \sigma_y) \tau_x + m \tau_x, \quad (20a)$$

$$H_Y = (v_2 k_x \sigma_x - v_1 k_y \sigma_y) \tau_x + m \tau_x, \quad (20b)$$

with the velocities v_1 and v_2 being given by

$$v_1 = \lambda_1 - \lambda_2, \quad v_2 = \lambda_1 + \lambda_2. \quad (21)$$

It is worthwhile to notice that this low-energy Hamiltonian agrees with the one derived based on a first-principle calculation and the Dirac theory of the TCI surface¹³.

Our Hamiltonian is capable to simulate various models by controlling m_ℓ . For instance, a massless Dirac cone emerges only at the Γ point by setting $m_0 = -2m_1$, as illustrated in Fig.3(a3) and (b3). Similarly a massless Dirac cone emerges only at the M point by setting $m_0 = 2m_1$, as illustrated in Fig.3(a4) and (b4).

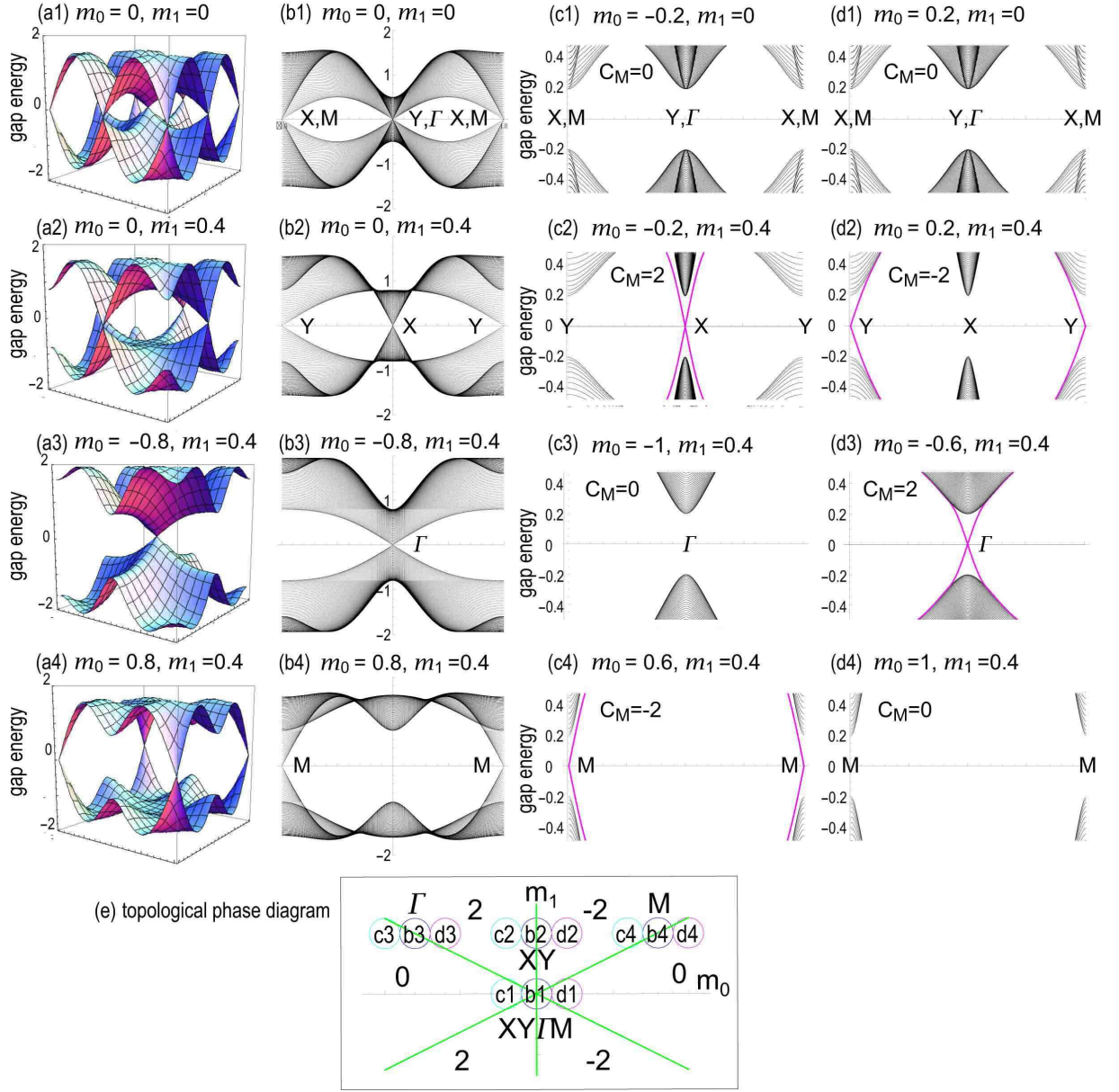


FIG. 3: **Band structure and topological phase diagram for square lattice.** (a) We show bird's eye views and (b) projected views of the bulk band structure. (c),(d) We show the band structure of nanoribbons, where the gapless edge states are depicted in the magenta curves. They emerge in topological insulators with nonzero mirror-Chern numbers. We have taken $\lambda_1 = 1$ and $\lambda_2 = -0.5$ in all figures. The values of m_0 and m_1 are indicated in each figure. The vertical axis is the energy in unit of λ_1 in all figures. The horizontal axes are $-\pi < k_x \leq \pi$, $-\pi < k_y \leq \pi$ in (a), $-\pi < k_x \leq \pi$ in (b), $-\pi < k \leq \pi$ in (c) and (d). (e) We present the topological phase diagram in the m_0 - m_1 plane. A green line represents a phase boundary. The numbers 0 and ± 2 are the mirror-Chern numbers. A circle with symbol such as c3 shows a point where the band structure is calculated in (c3).

The thin film is an insulator, since a gap is given to all Dirac points by the term $m_0\tau_x$. It is a topological insulator indexed by the mirror-Chern number in the absence of the electric field ($E_z = 0$). It is a symmetry protected topological number.

As we derive in the Methods, the mirror-Chern charge may be calculated²⁵ even for $E_z \neq 0$, and is given by

$$C_M(E_z) = \frac{1}{2}n_x n_y \frac{m}{\sqrt{m^2 + E_z^2}} \quad (22)$$

for each Dirac cone possessing the chirality $n_x n_y$ with m given by (18). When $E_z = 0$, it is reduced to

$$C_M = \frac{1}{2}n_x n_y \text{sgn}(m). \quad (23)$$

The total mirror-Chern number is quantized and given by

$$C_M = \text{sgn}(m_0 + 2m_1) + \text{sgn}(m_0 - 2m_1) - 2\text{sgn}(m_0). \quad (24)$$

We show the topological phase diagram in the (m_0, m_1) plane in Fig.3(e).

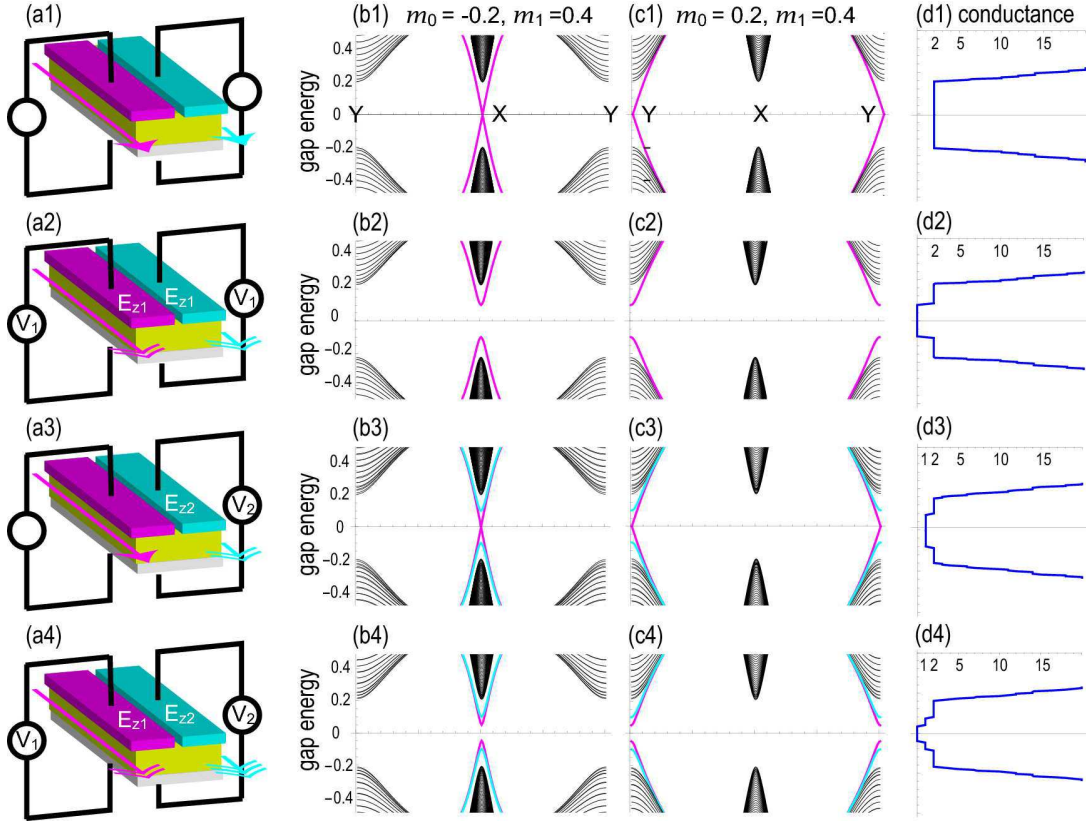


FIG. 4: **Multi-digit topological transistor, edge modes and conductance for square lattice.** (a) We apply electric fields independently to the right and left edges of a nanoribbon. (b), (c) Gapless edge modes emerge without electric fields since they are protected by the mirror symmetry. The gap can be controlled by electric field independently on the right and left edges. (d) We have calculated the conductance as a function of the gap energy. The conductance can take quantized values 0, 1 and 2 as in (d4), hence providing us with a basic mechanism of multi-digit topological transistor.

Nanoribbons: With the tight-binding Hamiltonian at hand, we are able to demonstrate the band structure of nanoribbons, as shown in Fig.3 for various values for parameters m_0 and m_1 . We have still set $E_z = 0$. We take the direction of nanoribbon as x -axis. The momentum component k_x in the bulk band gives the momentum k of nanoribbon, while the momentum component k_y is quantized. Accordingly, the X and M points are projected to the same momentum $k = \pi$, while the Y and Γ points are projected to $k = 0$. The projected view of the bulk band shown in Fig.3(b) is the same as the band structure of nanoribbon except for the edge states. Namely we can identify the edge states by comparing the projected band structure of the bulk band and the band structure of nanoribbon. The edge states are shown in magenta in Fig.3(c) and (d).

The bulk-edge correspondence works perfectly well. Indeed, gapless edge modes emerge when a nanoribbon has a nonzero mirror-Chern number. It is interesting that the gapless edge states emerge at $k = 0$ for $C_M > 0$ and at $k = \pi$ for $C_M < 0$. There are no edge states when the system is trivial ($C_M = 0$). There is exactly one to one correspondence between the mirror-Chern number and the appearance of edge states in the band structure of a nanoribbons.

The nonzero mirror-Chern number indicates "quantum mir-

ror Hall effects". However it is a highly nontrivial problem to experimentally detect the "mirror-Hall conductivity" since "mirror-Hall currents" convey neither charge nor spin. On the other hand, there emerge $|C_M|$ gapless states in the edges of a nanoribbon made of a topological insulator with the mirror-Chern number C_M . Without the electric field, these edge states transport merely the mirror charge M . Once we apply external electric field parallel to the nanoribbon direction, one edge state contributes one quantum unit to the electric conductance, as we show in Fig.4(d1). Hence we are able to determine the absolute value of the mirror-Chern number by measuring the conductance.

Electric field: We now switch on the electric field E_z between the front and back surfaces to control the edge modes and the conductance in nanoribbons [Fig.4(a)]. The mirror symmetry is broken by the electric field as in (10).

We show the band structure of a nanoribbon under the electric field E_z in Fig.4(b) and (c). The edge states become gapped due to the mixing of the right and left going edge states as a result of the mirror-symmetry breaking.

The gapless edge mode transports the electric current. We have calculated the conductance in the presence of E_z , which we show in Fig.4(d): See the Methods for derivation. The conductance near the Fermi energy is 2 for $E_z = 0$ [Fig.4(d1)]

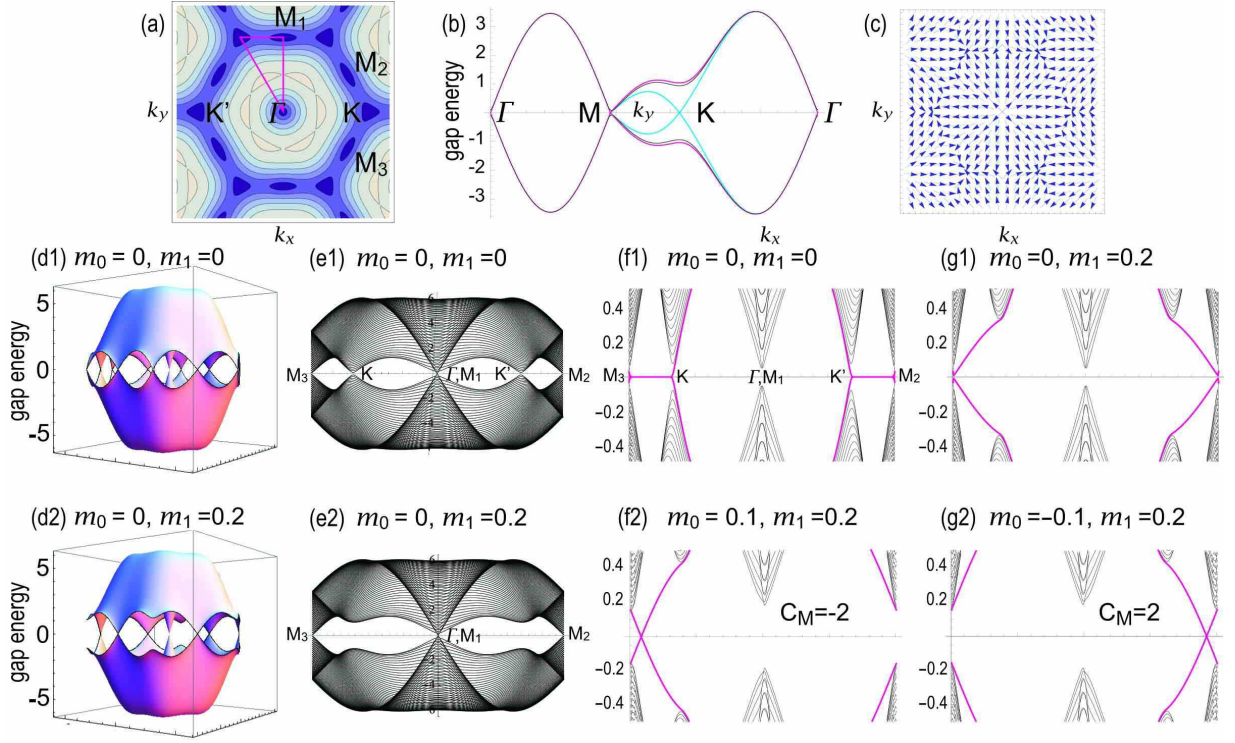


FIG. 5: **Band structure and spin direction for triangular lattice.** (a) We show a contour plot of the band structure of the Hamiltonian (6) on the triangular lattice. We have set $\lambda_1 = 0$, $m_1 = m_2 = 0$. The energy is lower in darker region. (b) We show the band structure along the lines shown in red in (a). We have set $\lambda_1 = 1$ in all three curves. Cyan curves are with $m_1 = m_2 = 0$. Magenta curves are with $m_1 = 0.2$, $m_0 = 0$. Black curves are with $m_1 = 0.2$, $m_0 = 0.1$. (c) We show the spin direction in the thin film with the C_6 symmetry for the whole Brillouin zone. (d) We present bird's eye views and (e) projected views of the bulk band structure. (f),(g) We present the band structure of nanoribbons, where the gapless edge states are depicted in the magenta curves. They emerge in topological insulators with nonzero mirror-Chern numbers. We have taken $\lambda_1 = 1$ in all figures. The values of m_0 and m_1 are indicated in each figure. The vertical axis is the energy in unit of λ_1 in all figures. The horizontal axes are $-\pi < k_x \leq \pi$, $-\pi < k_y \leq \pi$ in (d), $-\pi < k_x \leq \pi$ in (e), $-\pi < k \leq \pi$ in (f) and (g).

since the edge states are doubly degenerate. Once we turn on the electric field, the conductance falls to zero since the edge states disappear due to the anticrossing [Fig.4(d2)]. Namely, it acts as a field-effect transistor¹³. It is possible to apply different electric fields E_{z1} and E_{z2} to the right and left edge states [Fig.4(a)]. The conductance can be 0, 1 and 2, which forms a multi-digit field-effect topological transistor [Fig.4(d4)]. The conductance is quantized and topologically protected.

Triangular lattice with C_6 symmetry. We proceed to study the triangular lattice with the C_6 symmetry. Note that the triangular lattice has the hexagonal symmetry. By substituting $N = 3$ into the Hamiltonian (2), and taking only the nearest neighbor sites ($\ell = 1$), we obtain

$$A_x = -2\lambda_1 \left[\sin \frac{k_x}{2} \cos \frac{\sqrt{3}k_y}{2} + \sin k_x \right], \quad (25)$$

$$A_y = -2\sqrt{3}\lambda_1 \cos \frac{k_x}{2} \sin \frac{\sqrt{3}k_y}{2}. \quad (26)$$

We show the band structure in Fig.5. There are six massless Dirac cones, in which one Dirac cone resides at Γ , three Dirac cones at M points and two Dirac cones at K and K' points. In the vicinity of each Dirac cone, we obtain the low-energy

Dirac theory

$$A_x = v_x k_x, \quad A_y = v_y k_y, \quad (27)$$

with a set of velocities (v_x, v_y) to be $(-3\lambda_1, -3\lambda_1)$ for Γ , $(-\lambda_1, 3\lambda_1)$ for M_1 , $(3\lambda_1/2, 3\lambda_1/2)$ for K and K' . The chiralities of the Dirac cone at the Γ , K and K' points are identical, while three M points have opposite chirality. It is contrasted to the case of graphene, where the chiralities of K and K' points are opposite.

We show the band structure of nanoribbons in Fig.5. It is interesting that there exists a flat band in the region $-\pi \leq k \leq -\frac{2\pi}{3}$ and $\frac{2\pi}{3} \leq k \leq \pi$: See Fig.5(f1). The one is connecting the K and M points, and the other is connecting K' and M points.

In the similar manner to the square lattice, we introduce the mass term (7) to the Hamiltonian. The leading and the next leading terms are

$$m = m_0 + 4m_1 \sin \frac{k_x}{2} \left[\cos \frac{\sqrt{3}k_y}{2} - \cos \frac{k_y}{2} \right]. \quad (28)$$

By introducing the mass term, the Dirac cones at the K and K' points become gapped. The resultant spectrum has four

Dirac cones, in which one Dirac cone resides at the Γ point and the other three Dirac cones at the M points.

The total mirror-Chern number is given by

$$C_M = \text{sgn}(m_0 + 3\sqrt{3}m_1) + \text{sgn}(m_0 - 3\sqrt{3}m_1) - 2\text{sgn}(m_0). \quad (29)$$

This should be compared with the mirror-Chern number (24) in the square lattice with the C_4 symmetry. It follows that the phase diagram is essentially given by the same one as Fig.3(e).

We show the band structure of nanoribbons in Fig.5 in the presence of the mass term (28). The flat bands turn into the dispersive edge modes. The position of the edge modes is between the K (K') and $M_2 = M_3$ points when $C_M < 0$ ($C_M > 0$). As in the case of the square lattice, there is a perfect agreement between the mirror-Chern number and the edge states of nanoribbons, as dictated by the bulk-edge correspondence.

Discussions

The minimal tight-binding Hamiltonian of a TCI thin film is a four-band model in order to take into account the spin and pseudospin (surface) degrees of freedom. We have constructed such a model based on the symmetry analysis. The prominent features are that gapless Dirac cones emerge at all the high symmetric points and that we can provide them with gaps phenomenologically at our disposal.

We have analyzed the square lattice with the C_4 symmetry and the triangular lattice with the C_6 symmetry in details. The results may well describe the thin films made of the [001] surface (C_4 symmetry) and the [111] surface (C_6 symmetry) made of $\text{Pb}_x\text{Sn}_{1-x}\text{Te}$, by choosing the mass parameters appropriately. According to experimental observations and a first-principle calculation there are large gaps at the Γ and M points in the [001] surface^{8-10,13}. This is realized by taking a large value of m_1 in our model. On the other hand there are small gaps at the X and Y points, which is taken care of by introducing a small value of m_0 .

We may similarly discuss the square lattice with the C_2 symmetry with the mass term being $m = m_0 + m_1 \cos k_x$. When $m_0 = m_1$, there are Dirac cones only X and M points, as is consistent with theoretical results^{13,18} on the [110] surface of $\text{Pb}_x\text{Sn}_{1-x}\text{Te}$. The model with the C_3 symmetry is also constructed on the honeycomb lattice. We find Dirac cones at the K and K' points and two degenerated Dirac cones at the Γ point.

Our basic Hamiltonian consists of the SOI of the type $\sigma \cdot d_{ij}^\ell$ as in (2). We have made this choice since it reproduces the low-energy Dirac theory¹³. The same spectrum is obtained even if we take the SOI of the Rashba type $\sigma \times d_{ij}^\ell$ as in (1), although the low-energy Dirac theory now reads

$$H_X = (v_1 k_y \sigma_x + v_2 k_x \sigma_y) \tau_x + m \tau_y, \quad (30a)$$

$$H_Y = (v_2 k_y \sigma_x + v_1 k_x \sigma_y) \tau_x + m \tau_y, \quad (30b)$$

and different from (20). We predict that another TCI may be found in future, where the Rashba-type Hamiltonian (1) plays the basic role.

A TCI thin film may be used to design a nanodevice for topological electronics. Edge states can be gapped by applying electric field independently to the right and left edges. We have proposed a multi-digit field-effect topological quantum transistor with the use of gapless edge states of a TCI thin film nanoribbon. This could be a basic component of future topological quantum devices.

Methods

In this section we explain the discrete rotational symmetry C_N . We also describe how to calculate the mirror-Chern number and the conductance.

Symmetry. We have constructed the tight-binding Hamiltonian so that it is invariant under the discrete rotation symmetry C_N in addition to the mirror symmetry (9). The generator of C_N is

$$C_N = R_z \exp \left[-\frac{i\pi}{N} \sigma_z \right], \quad (31)$$

with the $\frac{2\pi}{N}$ -rotation of the momentum

$$R_z : \begin{pmatrix} k_x \\ k_y \end{pmatrix} \mapsto \begin{pmatrix} \cos \frac{2\pi}{N} & \sin \frac{2\pi}{N} \\ -\sin \frac{2\pi}{N} & \cos \frac{2\pi}{N} \end{pmatrix} \begin{pmatrix} k_x \\ k_y \end{pmatrix}. \quad (32)$$

We note that the C_N rotation rotates the direction of spin with π/N . The rotation angle is restricted to be $N = 2, 3, 4, 6$ due to the crystal group of the lattice symmetry. They corresponds to the rectangular lattice for $N = 2$, the hexagonal lattice for $N = 3$, the square lattice for $N = 4$, and the triangular lattice for $N = 6$.

Mirror-Chern number. According to a general scheme²⁵, the mirror-Chern charge is defined even for $E_z \neq 0$. With the use of the Matsubara Green function,

$$G(\mathbf{k}) = [i\omega - H(\mathbf{k})]^{-1}, \quad (33)$$

with $i\omega$ referring to the Matsubara frequency (ω : real), the mirror-Chern charge is calculated by²⁵

$$C_M = (2\pi)^{-2} \int d^2k \int_{-\infty}^{\infty} d\omega \Omega_M. \quad (34)$$

Here, $\Omega_M = \frac{1}{6} \varepsilon_{\mu\nu\rho} \text{Tr}[G\Gamma_\mu G\Gamma_\nu G\Gamma_\rho]$ and

$$\Gamma_x = \frac{1}{2} \{M, \partial_x G^{-1}\}, \quad \Gamma_y = \partial_y G^{-1}, \quad \Gamma_0 = \partial_0 G^{-1}, \quad (35)$$

with M the mirror-symmetry generator (9). The result is given by (22) for $E_z \neq 0$.

Conductance. In terms of single-particle Green's functions, the low-bias conductance $\sigma(E)$ at the Fermi energy E is given by²⁶

$$\sigma(E) = (e^2/h) \text{Tr}[\Gamma_L(E) G_D^\dagger(E) \Gamma_R(E) G_D(E)], \quad (36)$$

where $\Gamma_{R(L)}(E) = i[\Sigma_{R(L)}(E) - \Sigma_{R(L)}^\dagger(E)]$ with the self-energies $\Sigma_L(E)$ and $\Sigma_R(E)$, and

$$G_D(E) = [E - H_D - \Sigma_L(E) - \Sigma_R(E)]^{-1}, \quad (37)$$

with the Hamiltonian H_D for the device region. The self-energy $\Sigma_{L(R)}(E)$ describes the effect of the electrode on the electronic structure of the device, whose the real part results in a shift of the device levels whereas the imaginary part provides a life time. It is to be calculated numerically^{24,27–30}.

Acknowledgements

I am very much grateful to N. Nagaosa, L. Fu and T. H. Hsieh for many helpful discussions on the subject. This work was supported in part by Grants-in-Aid for Scientific Research

from the Ministry of Education, Science, Sports and Culture No. 22740196.

Additional information

Competing financial interests: The author declares no competing financial interests.

Author contributions: M. E. performed all calculations and made all contribution to the preparation of this manuscript.

- ¹ Hasan, M. Z. and Kane, C. , Topological insulators. *Rev. Mod. Phys.* **82**, 3045 (2010).
- ² Qi, X.-L. and Zhang, S.-C. Topological insulators and superconductors. *Rev. Mod. Phys.* **83**, 1057 (2011).
- ³ Kane C. L. and Mele E. J. , $Z(2)$ topological order and the quantum spin Hall effect , *Phys. Rev. Lett.* **95** 146802 (2005).
- ⁴ Fu, L. Kane, C. L. and Mele, E. J. Topological Insulators in Three Dimensions, *Phys. Rev. Lett.* **98**, 106803 (2007)
- ⁵ Qi, X.-L. Hughes, T. L. and Zhang, S.-C., Topological field theory of time-reversal invariant insulators, *Phys. Rev. B* **75** 121306 (2008)
- ⁶ Fu, L. Topological crystalline insulators. *Phys. Rev. Lett.* **106**, 106802 (2011).
- ⁷ Hsieh, T. H. *et.al.* Topological crystalline insulators in the SnTe material class. *Nat. Comm.* **3**, 982 (2012).
- ⁸ Tanaka, Y. *et.al.* Experimental realization of a topological crystalline insulator in SnTe. *Nat. Phys.* **8**, 800 (2012).
- ⁹ Xu, S.Y. *et.al.* Observation of a topological crystalline insulator phase and topological phase transition in $\text{Pb}_{1-x}\text{Sn}_x\text{Te}$. *Nat. Com.* **3**, 1192 (2012).
- ¹⁰ Dziawa, P. *et.al.* Topological crystalline insulator states in $\text{Pb}_{1-x}\text{Sn}_x\text{Se}$. *Nat. Mat.* **11**, 1023 (2012).
- ¹¹ Tanaka, Y. *et.al.*, Two types of Dirac-cone surface states on (111) surface of topological crystalline insulator SnTe. *cond-mat/arXiv:1312.2803*
- ¹² Polley, C. M. *et.al.* Observation of topological crystalline insulator surface states on (111)-oriented $\text{Pb}_{1-x}\text{Sn}_x\text{Se}$ films. *cond-mat/arXiv:1312.3226*
- ¹³ Liu, J. *et.al.* Spin-filtered edge states with an electrically tunable gap in a two-dimensional topological crystalline insulator. *Nat. Mat.* **13** 178 (2014).
- ¹⁴ Fang, C. Gilbert, M. J. and Bernevig, B. A., Large-Chern-number quantum anomalous Hall effect in thin-film topological crystalline insulators. *Phys. Rev. Lett.* **112**, 046801 (2014).
- ¹⁵ Liu, J. Duan, W. and Fu, L. Two types of surface states in topological crystalline insulators. *Phys. Rev. B* **88**, 241303(R) (2013).
- ¹⁶ Fang, C. *et.al.* Theory of quasiparticle interference in mirror-symmetric two-dimensional systems and its application to surface states of topological crystalline insulators. *Phys. Rev. B* **88**, 125141 (2013).
- ¹⁷ Y. Okada, Y. *et.al.* Observation of Dirac Node Formation and Mass Acquisition in a Topological Crystalline Insulator. *Science* **341** 1496 (2013).
- ¹⁸ Safaei, S. Kacman, P. and Buczko, R. Topological crystalline insulator (Pb,Sn)Te: Surface states and their spin polarization. *Phys. Rev. B* **88** 045305 (2013).
- ¹⁹ Wojek, B. M. *et.al.* Spin-polarized (001) surface states of the topological crystalline insulator $\text{Pb}_{0.73}\text{Sn}_{0.27}\text{Sem}$. *Phys. Rev. B* **87** 115106 (2013).
- ²⁰ Wang, Y. J. *et.al.* Nontrivial spin texture of the coaxial Dirac cones on the surface of topological crystalline insulator SnTe. *Phys. Rev. B* **87** 235317 (2013).
- ²¹ C.Y. Teo, J. C. Y. Fu, L. and Kane, C. L. Surface states and topological invariants in three-dimensional topological insulators. Application to $\text{Bi}_{1-x}\text{Sb}_x$. *Phys. Rev. B* **78**, 045426 (2008).
- ²² Takahashi, R and Murakami, S. Gapless interface states between topological insulators with opposite Dirac velocities. *Phys. Rev. Lett.* **107**, 166805 (2011).
- ²³ Nielsen, H. B. Ninomiya, M. A no-go theorem for regularizing chiral fermions. *Phys. Lett. B* **105**, 219 (1981).
- ²⁴ Ezawa, M. Quantized conductance and field-effect topological quantum transistor in silicene nanoribbons. *Appl. Phys. Lett.* **102**, 172103 (2013).
- ²⁵ Ezawa, M. Symmetry protected topological charge in symmetry broken phase: spin-Chern, spin-valley-Chern and mirror-Chern numbers. *cond-mat/arXiv:1310.3536* (to be published in *Phys. Lett. A*, DOI:10.1016/j.physleta.2014.02.014).
- ²⁶ Datta, S. *Electronic Transport in Mesoscopic Systems* (Cambridge University Press, Cambridge, England, 1995); *Quantum Transport: Atom to Transistor* (Cambridge University Press, England, 2005)
- ²⁷ Sancho, M. P. L., Sancho, J. M. L. and Rubio, J. Highly convergent schemes for the calculation of bulk and surface Green functions. *J. Phys. F: Met. Phys.* **15**, 851 (1985).
- ²⁸ Muñoz-Rojas, F., Jacob, D. Fernández-Rossier, J. and Palacios, J. J. Coherent transport in graphene nanoconstrictions. *Phys. Rev. B* **74**, 195417 (2006).
- ²⁹ Zárbo, L. P. and Nikolić, B. K. Spatial distribution of local currents of massless Dirac fermions in quantum transport through graphene nanoribbons. *EPL*, **80** 47001 (2007); D. A. Areshkin and B. K. Nikolić, I-V curve signatures of nonequilibrium-driven band gap collapse in magnetically ordered zigzag graphene nanoribbon two-terminal devices. *Phys. Rev. B* **79**, 205430 (2009).
- ³⁰ Li, T. C., and Lu, S.-P, Quantum conductance of graphene nanoribbons with edge defects. *Phys. Rev. B* **77**, 085408 (2008).